

Spectroscopic Optical Coherence Tomography and Microscopy

Amy L. Oldenburg, Chenyang Xu, *Member, IEEE*, and Stephen A. Boppart, *Senior Member, IEEE*

Abstract—Imaging biological tissues using optical coherence tomography is enhanced with spectroscopic analysis, providing new metrics for functional imaging. Recent advances in spectroscopic optical coherence tomography (SOCT) include techniques for the discrimination of endogenous tissue types and for the detection of exogenous contrast agents. In this paper, we review these techniques and their associated signal processing algorithms, while highlighting their potential for biomedical applications. We unify the theoretical framework for time- and frequency-domain SOCT and introduce a noise correction method. Differences between spectroscopic Mie scatterers are demonstrated with SOCT, and spectroscopic imaging of macrophage and fibroblast cells in a 3-D scaffold is shown.

Index Terms—Biophotonics, functional imaging, molecular imaging, optical coherence tomography, spectroscopy, tissue.

I. INTRODUCTION

From distant astronomical objects to our daily environment, optical spectroscopy is an indispensable tool for understanding the structure of matter and for chemical and structural sensing. There are a variety of optical processes amenable to spectroscopic analyses that are being increasingly utilized for sensing in biomedicine. Optical absorption spectroscopy has enjoyed widespread use in blood oximetry [1]. Raman spectroscopy detects molecules based on their vibrations, promoting recent advances in cancer detection [2]. In addition to chemical sensitivity, linear light scattering spectra are sensitive to object structure, such as scatterer size, shape, and geometrical distribution, which can provide additional functional information. For example, techniques such as light scattering spectroscopy [3] and

Manuscript received September 6, 2007; revised October 4, 2007. This work was supported in part by the National Institutes of Health under the Roadmap Initiative, in part by the National Institute of Biomedical Imaging and Bioengineering under Grant 1 R21 EB005321, Grant 1 R01 EB005221, and Grant 1 R01 EB001777, in part by the National Science Foundation under Grant BES 03-47747, Grant BES 05-19920, and Grant BES 06-19257, and in part by the Siteman Center of Cancer Nanotechnology Excellence, through the University of Illinois Center for Nanoscale Science and Technology under Grant NCI U54-CA119342-01. Additional information can be found at <http://biophotonics.uiuc.edu>.

A. L. Oldenburg is with the Beckman Institute for Advanced Science and Technology, University of Illinois at Urbana-Champaign, Urbana, IL 61801 USA (e-mail: oldenbrg@uiuc.edu).

C. Xu was with the Department of Electrical and Computer Engineering, University of Illinois at Urbana-Champaign, Urbana, IL 61801 USA. He is now with LightLab Imaging, Westford, MA 01886 USA (e-mail: xuchenyang@gmail.com).

S. A. Boppart is with the Beckman Institute for Advanced Science and Technology, also with the Departments of Electrical and Computer Engineering, Bioengineering, and Internal Medicine, University of Illinois at Urbana-Champaign, Urbana, IL 61801 USA, and also with the Mills Breast Cancer Institute, Carle Foundation Hospital, Urbana, IL 61801 USA (e-mail: boppart@uiuc.edu).

Color versions of one or more of the figures in this paper are available online at <http://ieeexplore.ieee.org>.

Digital Object Identifier 10.1109/JSTQE.2007.910292

low-coherence interferometry [4] have shown promise toward early-stage cancer detection by monitoring dysplastic cellular changes.

A natural extension of chemical and structural sensing is molecular and functional imaging, that is, imaging the distribution of specific molecular species and physiological processes. This powerful new paradigm is of great interest in many areas of biomedical imaging [5]. One promising optical molecular imaging method is coherent anti-Stokes Raman scattering (CARS) microscopy [6]. CARS is a nonlinear optical process for assessing molecular vibrational spectra, which exhibits larger signal strengths than spontaneous Raman scattering. Interferometric CARS imaging methods [7]–[9] provide depth-ranging capabilities, which have potential for 3-D tomographic imaging of endogenous molecules. Thus, CARS imaging may allow for the *in situ* detection of disease based upon its molecular signature. Future simplifications in the laser hardware, such as the use of a single laser source as proposed in [7], and recent developments in catheter technology [10], are promising for the biomedical application of CARS imaging. Also, molecular *contrast* imaging is achieved by using exogenous agents (including dyes and quantum dots for fluorescence microscopy), which are chemically modified to target specific biomolecules.

Optical coherence tomography (OCT) is a biomedical imaging modality [11], which is being increasingly used for clinical imaging in areas including ophthalmology, gastroenterology, cardiology, and oncology. OCT performs imaging by interferometrically detecting singly backscattered light, to render a depth-resolved image of biological tissues. Not surprisingly, it was not long after the development of OCT that the first spectroscopic OCT (SOCT) imaging was described [12] and, subsequently, demonstrated endogenous contrast in tissue imaging [13]. Also, new classes of exogenous contrast agents are currently being developed [14], because OCT cannot sense incoherent light emitted from standard fluorescent probes.

Because the imaging light used in OCT is necessarily broadband, spectral analysis of each voxel in the OCT image yields new metrics, opening many doors for molecular and functional imaging. SOCT may provide the ability to exogenously label tissues using disease-specific markers, as well as the ability to detect endogenous tissue morphologies indicative of disease such as nuclear size enlargement or cell type. In this paper, we review the relevant SOCT theory and processing algorithms, then focus on applications for tissue analysis and functional imaging, and lastly discuss the use of SOCT contrast agents for applications in molecular contrast imaging.

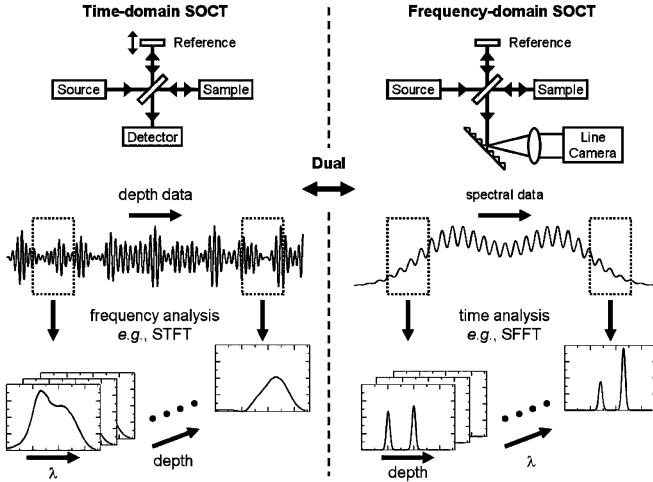


Fig. 1. Spectroscopic OCT imaging using time-domain (left) or frequency-domain (right) interferometry. Short-time and short-frequency Fourier transforms are performed on the OCT interferograms to create 2-D SOCT signals indexed by wavelength (λ) and depth in the object.

II. SOCT THEORY

A. Time-Frequency Duality

To appreciate the capabilities of SOCT imaging, let us review the fundamental aspects of SOCT signal theory. First, we present the basic SOCT concepts with more intuitive time-domain interferometry, then translate these concepts to frequency-domain interferometry, which is more commonly employed in OCT imaging today.

1) *Time-Domain SOCT*: The central component of OCT is an interferometer (most commonly a Michelson interferometer), where a light beam is divided into two paths (reference and sample arms), recombined, and detected with a photodetector (Fig. 1) [15]. The reference arm consists of a moving reflecting mirror that scans the optical delay τ . The sample arm consists of an imaging lens to focus light within the object and concomitantly collect the backscattered light. To build up a 2-D or 3-D image, the light beam is laterally translated across the object while acquiring successive depth scans by each sweep of the moving reference mirror.

The intensity S_{OCT} incident on the photodetector at the output of the interferometer for one depth scan is described by

$$\begin{aligned} S_{\text{OCT}}(\tau) &= \langle |E_R(t - \tau) + E_S(t)|^2 \rangle \\ &= \langle |E_R|^2 \rangle + \langle |E_S|^2 \rangle + 2\text{Re} \langle E_S^*(t) E_R(t - \tau) \rangle \end{aligned} \quad (1)$$

where E_R and E_S are the electric fields returned from the reference and sample, respectively, and brackets indicate averaging over time t . The last term in (1) is the mutual coherence function between the sample and reference electric fields, and the first two terms contribute a constant offset equal to the average light intensity. For a stationary sample object, the temporal statistics of E_R and E_S are identical to the original light source, and, thus, the mutual coherence function is equivalent to an autocorrelation function convolved with the backscattering amplitude (i.e.,

scattering potential) from the object. (For simplicity, we neglect dispersion, which modifies the spectral phase [15].) The consequence is that the reference and sample fields interfere only if their relative time delay is less than the coherence time t_c of the light source. In this way, as the reference field is scanned in τ , it interferes with backscattering structures within the object at associated depth positions $z = (\tau \pm t_c) c/n$, where c is the speed of light *in vacuo* and n is the refractive index of the object.

By using light with a shorter t_c , the interference signals become more localized in z to specific backscattering structures within the object. The axial OCT image resolution is, thus, given by the coherence length $l_c = t_c c/n$. In general, t_c (and l_c) are inversely proportional to the source bandwidth $\Delta\omega_0$ because of the time-frequency Fourier relationship according to the Wiener-Khinchine theorem [16]

$$\begin{aligned} I(\omega) &= |E(\omega)|^2 \propto \int_{-\infty}^{\infty} \langle E^*(t) E(t - \tau) \rangle \exp(-i\omega\tau) d\tau \\ &= F \{ \langle E^*(t) E(t - \tau) \rangle \} \end{aligned} \quad (2)$$

where $I(\omega)$ is the spectral intensity, ω the angular frequency, and F the Fourier transform. Equation (2) is subject to an uncertainty principle, which is an inherent tradeoff between spectral and spatial (temporal) resolution, where improvement in one necessitates degradation in the other. This is why broad bandwidth light sources corresponding to short temporal autocorrelation widths t_c are used for OCT imaging. The uncertainty principle is important for SOCT as well, because quantifying the spectral response with a resolution of $\Delta\omega$ is equivalent to reducing the light bandwidth to $\Delta\omega$ from the total bandwidth $\Delta\omega_0$.

In fact, one of the most basic SOCT processing methods consists of applying a short-time Fourier transform (STFT) to the interferogram over a time-delay window centered at τ_0 with width $\Delta\tau$

$$\begin{aligned} I(\omega, \tau_0) &= |I(\omega, \tau_0)| \exp(i\phi(\omega, \tau_0)) \\ &= \frac{2}{\Delta\tau} \int_{\tau_0 - \Delta\tau/2}^{\tau_0 + \Delta\tau/2} \text{Re} \langle E_S^*(t) E_R(t - \tau) \rangle \exp(-i\omega\tau) d\tau \\ &= \text{STFT} \{ S_{\text{OCT}}(\tau) - \langle |E_R|^2 \rangle \} \end{aligned} \quad (3)$$

where Re indicates the real part, and ϕ is the phase of the complex time-frequency distribution $I(\omega, \tau_0)$. (The sample field intensity is assumed to be negligible compared to $|E_R|^2$). Because the interferogram is modulated by a carrier frequency proportional to the light spectrum (as shown by (2)), the SOCT signal $I(\omega, \tau_0)$ associates a spectrum with the windowed region in the object. Also, we note that the parameters of I are typically converted from frequency ω to wavelength λ and from time delay τ to object depth z , as shown in Fig. 1. Based on (2) and (3), we can approximate the spectral resolution $\Delta\omega$ in terms of the light source bandwidth $\Delta\omega_0$ as

$$\frac{\Delta\lambda}{\lambda_0} = \frac{\Delta\omega}{\Delta\omega_0} \approx \frac{t_c}{\Delta\tau} = \frac{l_c}{\Delta z} \quad (4)$$

where a larger temporal window $\Delta\tau$ allows for finer spectral resolution $\Delta\omega$ (or $\Delta\lambda$ in terms of wavelength), but at the expense of spatial resolution Δz . The approximation in (4) depends on the

exact lineshape of the spectrum and on the time-frequency transformation used (of which the STFT is only one). In Section II-B, we will compare the particular merits of several time-frequency distributions.

Unlike a spectrometer where only magnitude is recorded, SOCT can record both the magnitude and phase information. One useful phase-based metric is the relative group delay (RGD) t_g , which is defined as the phase differential with respect to frequency (i.e., phase dispersion). This can be computed in a manner that is robust to noise by the following expression [17]:

$$t_g(\omega, \tau_0) \equiv \frac{\partial \phi(\omega, \tau_0)}{\partial \omega} = \frac{\text{STFT}\{\tau(S_{\text{OCT}}(\tau) - \langle |E_R|^2 \rangle)\}}{\text{STFT}\{S_{\text{OCT}}(\tau) - \langle |E_R|^2 \rangle\}}. \quad (5)$$

2) *Frequency-Domain SOCT*: So far, we have demonstrated the relationship between the time-domain OCT interferogram and the spectroscopic response of the object. However, a significant signal-to-noise ratio advantage has been demonstrated when using frequency-domain interferometry for OCT [18], [19]. Frequency-domain SOCT can be implemented using either a spectrometer as the detector or a wavelength-swept light source, such as in [20]. In either case, the reference mirror is fixed and the measured spectrum $S_{\text{OCT}}(\omega)$ is

$$\begin{aligned} S_{\text{OCT}}(\omega) &= |E_R(\omega) + E_S(\omega)|^2 \\ &= |E_R(\omega)|^2 + |E_S(\omega)|^2 + 2\text{Re}(E_S^*(\omega) E_R(\omega)) \end{aligned} \quad (6)$$

where $E_i(\omega) = F\{E_i(t)\}$. The last term in (6) is a modulation term, which is proportional to the Fourier transform of the depth-dependent backscattering amplitude of the object, and weighted by the spectral intensity of the source $I(\omega)$, as shown in [21]. Thus, point scatterers at various depths z within the object are encoded as frequency modulations $\cos(\omega\Delta\tau)$ with period $1/\Delta\tau$ on top of $I(\omega)$, where $\Delta\tau$ is the relative time delay between the field from the scatterer and the reference field (and is directly proportional to z).

The ability to perform SOCT using frequency-domain OCT was first demonstrated by [22]. Analogous to the STFT for time-domain OCT, a short-frequency Fourier transform (SFFT) was applied to the spectral interferogram

$$\begin{aligned} I(\omega_0, \tau) &= |I(\omega_0, \tau)| \exp(i\phi(\omega_0, \tau)) \\ &= \frac{1}{\pi\Delta\omega} \int_{\omega_0 - \Delta\omega/2}^{\omega_0 + \Delta\omega/2} \text{Re}(E_S^*(\omega) E_R(\omega)) \exp(i\omega\tau) d\omega \\ &= \text{SFFT}\{S_{\text{OCT}}(\omega) - |E_R(\omega)|^2\}. \end{aligned} \quad (7)$$

This provides an SOCT signal $I(\omega_0, \tau)$, which allows us to associate the depth- (or equivalently τ -) dependent backscattering in the object with frequency components in the spectral window $\omega_0 - \Delta\omega/2$ to $\omega_0 + \Delta\omega/2$.

We can immediately observe the analogies between the time- and frequency-domain OCT signals, i.e., (1) and (6), respectively, and the SOCT signals, i.e., (3) and (7), respectively, as illustrated in Fig. 1. The choices of window size and time-frequency transformation (TFT) are dictated by the questions that one wishes to answer. For example, sensing a tissue type

or contrast agent with a known wavelength dependence may require a certain spectral resolution. As we will show, the TFT can be tailored to provide a slightly more compact time-bandwidth product. However, the available information is independent of these choices, and solely determined by the bandwidth of the light source.

B. Time-Frequency Transformations

The 2-D time-frequency representation is, often, a more compact and intuitive way to represent 1-D signals, such as how a musical score represents a time sequence of individual notes. This is the goal of SOCT, that is, to provide an intuitive representation of the object that answers a predefined question. The choice of TFT to convert the 1-D OCT signal is highly dependent on this question [23]. TFTs can be divided into two general classes: linear transformations, which are fully invertible such as the STFT and the Morlet-wavelet transforms (MWT) [24], and nonlinear transformations such as the Cohen's class TFTs, which are bilinear [25].

While the STFT shown in (3) uses a rectangular window, the more general form of the STFT of a signal f is written in terms of an arbitrary window function h as follows:

$$I(\omega, \tau_0) = F\{f(\tau) h(\tau_0 - \tau)\}. \quad (8)$$

To avoid undesired artifacts in the spectral response that arise from a rectangular window, a smooth envelope function such as a Gaussian or Hamming window is typically chosen for h . Similarly, the MWT converts f into a time-frequency distribution by integration with an orthonormal basis set of wavelets Ψ

$$I(a, \tau_0) = \frac{1}{\sqrt{a}} \int_{-\infty}^{\infty} f(\tau) \Psi\left(\frac{\tau - \tau_0}{a}\right) d\tau \quad (9)$$

where the scale a is directly proportional to ω . Because the wavelets are scaled logarithmically rather than linearly in frequency, the MWT is more appropriate for signals spanning multiple octaves [24] (although this is not usually the case in OCT). Another potential advantage of the MWT is that it avoids windowing artifacts, and has proven utility in *in vivo* SOCT [13].

The Wigner-Ville distribution (WVD) is a bilinear transform, which is one of the simplest Cohen's class TFTs

$$I(\omega, \tau_0) = F\left\{f\left(\tau_0 - \frac{\tau}{2}\right) f^*\left(\tau_0 + \frac{\tau}{2}\right)\right\}. \quad (10)$$

Although bilinear transforms can better concentrate the time-frequency response (Table I), they are also subject to cross-terms, where the signal f effectively interferes with itself, which can be difficult to interpret. These cross-terms can be reduced using low-pass filtering methods such as the smoothed-pseudo WVD, particularly since OCT signals typically have low fractional bandwidths and, thus, the cross-terms are found outside the signal band [23]. Interestingly, it has been recognized that (10) is equivalent to the Fourier transform of the OCT interference term in (1) if f is the electric field E [26], and, in this sense, the WVD self-interference terms contain information about the coherence of the light source. However, in the following computations, we will use the measured signal $f = S_{\text{OCT}} - |E_R|^2$

TABLE I
TIME-FREQUENCY RESOLUTIONS OF TFTS

		STFT	MWT	WVD
Relative time spread	$\left(\frac{\Delta\tau}{t_c}\right)$	1.2	1.5	0.74
Relative frequency spread	$\left(\frac{\Delta\omega}{\Delta\omega_0}\right)$	2.0	2.4	1.4
Relative time-frequency product	$\left(\frac{\Delta\omega\Delta\tau}{\Delta\omega_0 t_c}\right)$	2.4	3.5	1.0

(where the reference intensity offset is measured by blocking the sample beam path).

Comparisons between the time and frequency spreads of time-frequency distributions produced with these three TFTs using an optimized set of parameters (window sizes, scales, etc.) are shown in Table I. These were computed by modeling the OCT signal from a point scatterer with a flat frequency response and Gaussian light spectrum [23]. The most compact time-bandwidth product in this scenario is achieved with the WVD. However, the STFT is less prone to artifacts and more robustly reproduces the correct light spectrum. Considering this, it has been suggested that for applications where fine time-frequency resolution is required (such as closely packed spectroscopic scatterers), a Cohen's class TFT is preferred, and, for other applications, such as spectral estimation of absorption (where the cumulative response of the light traveling through the medium need not be tightly resolved), the STFT should be employed [23].

We note that while the aforementioned discussion involves general methods for converting OCT data into time-frequency space, some additional methods of interpretation are still required to answer the question of interest, such as spectral pattern analysis. In fact, integrated model-based approaches can be a more powerful means of achieving a specific goal. Some examples of each of these will be presented in the rest of the paper.

C. Spectroscopic Tissue Transport

So far, the discussion has neglected any mention of the physical mechanisms of light transport, or the meaning of the "spectroscopic response" obtained from the SOCT analysis. It is instructive to write the response empirically in terms of transfer functions $H_i(\omega)$ acting on the laser field $E_0(\omega)$

$$E_r(\omega) = H_{sr}(\omega) E_0(\omega)$$

$$E_s(\omega, z) = H_{ss}(\omega) H_a(\omega, z) H_b(\omega, z) E_0(\omega) \quad (11)$$

where H_{sr} and H_{ss} are the transfer functions of the system optics traversed by the reference and sample arm beams, respectively, H_a accounts for the attenuation by the object as the light travels to depth z and back out again, and H_b accounts for the spectral backscattering of the scatterer at depth position z . All of the time-frequency object information is contained in the product $H_a H_b$, which can be separated from the other spectral terms by normalizing against the SOCT signal from a mirror, Lambertian surface, or other object with known spectroscopic

response. H_a and H_b also contain spectral phase terms, which, according to (5), are subject to material dispersion and scattering dispersion, respectively. For simplicity, in the rest of Section II, we will neglect these dispersive effects by assuming that the transfer functions H are positive and real-valued.

The attenuation H_a can be described in terms of the object scattering and absorption coefficients μ_s and μ_a , respectively, using Beer's law

$$H_a(\omega, z) = \exp\left(-\int_{z_s}^z (\mu_s(\omega, z') + \mu_a(\omega, z')) dz'\right) \quad (12)$$

where z_s is the position of the object surface. Note that there is a distinction between total scattering (μ_s), which attenuates the propagating light beam, and backscattering (H_b), which returns light to the OCT interferometer; these may exhibit different spectral profiles. Usually, the spectroscopic attenuation coefficient ($\mu_t = \mu_s + \mu_a$) is estimated over a window from $z - \Delta z/2$ to $z + \Delta z/2$ by computing the depth differential

$$\mu_t(\omega, z) = \frac{1}{\Delta z} \ln\left(\frac{H_a(\omega, z - \Delta z/2)}{H_a(\omega, z + \Delta z/2)}\right). \quad (13)$$

Because of their differential nature, attenuation measurements are somewhat error-prone. In one study, using weakly-scattering tissue phantoms (attenuation dominated by absorption), absorption coefficients as low as 5/cm were detected with a precision that improved with increasing Δz [27]. However, attenuation measurements are further complicated by the presence of scattering structures, which modulate H_b in z , obscuring the measurement of H_a . Conversely, measurements of the depth-dependent backscattering H_b are obscured, at large z , when the wavelength dependence of H_a becomes significant. Near the object surface, H_b will dominate and can be measured directly, and, in fact, this surface response can be used to calibrate $H_b(\omega)$ in objects where it is depth-independent ($H_b(\omega, z) = H_b(\omega)R_b(z)$) [28].

Equations (12) and (13) neglect the effects of multiple light scattering, which become significant when imaging a specimen over a depth greater than the photon mean free path length [29]. Multiply scattered light that is reflected back into the OCT imaging system causes a greater signal to be observed at these larger depths, resulting in underestimation of the attenuation coefficient if (13) is used [30]. Thus, a multiple-scattering model, such as in [31] may be warranted for accurate estimation of the scattering coefficient.

The rationale for separating the absorption and scattering terms in (12) is to aid in situations where one wishes to sense an absorbing chromophore (such as melanin, hemoglobin, or exogenous dyes) within a scattering-dominated medium (which is the case for most tissue types at near-infrared (NIR) wavelengths). If the absorbers are linear in concentration (Beer-Lambert) and the scatterers are independent, their coefficients are separable as follows:

$$\mu_a(\omega, z) = \varepsilon_a(\omega) \rho_a(z)$$

$$\mu_s(\omega, z) = \varepsilon_s(\omega) \rho_s(z) \quad (14)$$

where ε_i are molar absorption/scattering coefficients and ρ_i are the concentrations of the absorbers/scatterers. The spatially averaged $\varepsilon_s(\omega)$ for many tissues is typically monotonic in the NIR. (However, because (14) uses the assumption that the scattering spectrum is depth-independent, it may not always be appropriate for layered tissues.) Against this background, it is possible to detect chromophores with a more structured spectrum $\varepsilon_a(\omega)$. Prior measurements of $\varepsilon_a(\omega)$ and $\varepsilon_s(\omega)$ can, therefore, be used with (12) and (14) to back out the spatial distributions $\rho_a(z)$ and $\rho_s(z)$ in a least-squares sense from OCT images [28].

In contrast to the cumulative response H_a , H_b is a localized backscattering response that can be highly spectrally modulated. It is sensitive to the scatterer geometry and refractive index according to the Mie theory, and, as such, is a promising metric for tissue analysis. Further discussion of H_b will be postponed until Section III.

D. SOCT Noise Correction

Various methods for denoising time- and frequency-domain OCT signals include bandpass filtering or wavelet denoising. However, some component of shot noise, which is white noise, will remain in the signal band. Although this noise has a zero mean value added to the detected signal, after taking the magnitude of a time-frequency distribution, the expectation value becomes nonzero, which is particularly troublesome in applications with low signal-to-noise ratio (such as sensing low dosages of contrast agents).

The detected OCT signal in the presence of shot noise can be approximated

$$S_{\text{OCT}} \approx 2\text{Re}(E_S^* E_R) + |E_R|^2 + \tilde{\sigma} |E_R| \quad (15)$$

where $\tilde{\sigma}$ is a real-valued zero-mean Gaussian variable that adds shot noise proportional to the reference field strength $|E_R|$ (in the usual case, where $|E_R| \gg |E_S|$). We omitted the arguments to emphasize that this expression is valid for both time- and frequency-domain OCT. The goal of SOCT analysis is to isolate the object-specific time-frequency response $H_a H_b$, which we will write as H_{ab} for simplicity. To accomplish this, it is necessary to acquire three OCT data sets using the same sampling in transverse coordinate x and in time or frequency, where $S_O(x, \tau, \omega)$ is an OCT image of the object, $S_R(x, \tau, \omega)$ is acquired while blocking the sample beam (measuring the reference beam only), and $S_M(x, \tau, \omega)$ is an OCT image of an object with a known response (such as a mirror). Even though x has no physical meaning for S_R because the object path is blocked, it reminds us that S_R must be sampled in the same way as S_O , so that the background statistics may be estimated.

Using (11) and (15), we find

$$\begin{aligned} \text{TFT}(S_O) &= 2H_{ss}(\omega) H_{sr}(\omega) H_{ab}(\omega, \vec{r}) |E_0(\omega)|^2 \\ &\quad + H_{sr}(\omega)^2 |E_0(\omega)|^2 + \tilde{\sigma} H_{sr}(\omega) |E_0(\omega)| \\ \text{TFT}(S_R) &= H_{sr}(\omega)^2 |E_0(\omega)|^2 + \tilde{\sigma} H_{sr}(\omega) |E_0(\omega)| \\ \text{TFT}(\overline{S_R}) &= H_{sr}(\omega)^2 |E_0(\omega)|^2 \end{aligned} \quad (16)$$

where \vec{r} is the (x, z) location in the object, and the bar over S_R indicates averaging over all x . Writing the known transfer function of the reference object as H_{abm} , we can, then, solve for H_{ab} as follows:

$$\begin{aligned} H_{ab}(\omega, \vec{r}) &= H_{abm}(\omega, \vec{r}) \frac{\left\langle \left| \text{TFT} \left(\frac{S_O - \overline{S_R}}{S_R} \right) \right| \right\rangle - \left\langle \left| \text{TFT} \left(\frac{S_R - \overline{S_R}}{S_R} \right) \right| \right\rangle}{\left\langle \left| \text{TFT} \left(\frac{S_M - \overline{S_R}}{S_R} \right) \right| \right\rangle - \left\langle \left| \text{TFT} \left(\frac{S_R - \overline{S_R}}{S_R} \right) \right| \right\rangle} \end{aligned} \quad (17)$$

where TFT is an arbitrary linear time-frequency transformation such as (8) or (9). The brackets indicate spatial averaging, which should be performed independently for each term to ensure the correct estimation of the offset due to noise. (In practice, averaging over multiple speckles is necessary to smooth the speckle-modulated spectral response [32].) We note that if only relative measurements of H_{ab} are required (such as for contrast agent detection), S_M may be measured from any arbitrary fixed object.

The utility of (17) has been experimentally verified using a line-camera-based frequency-domain OCT system described previously [33]. In brief, this system consists of a Ti:Sapphire light source (spectrum in Fig. 1), a single-mode fiber interferometer, a computer-controlled stage for transverse scanning, and a camera (Dalsa Piranha 2) operated at 7.5 kHz. A set of band- and low-pass filters (Edmund Optics) were individually placed in the sample beam path before a Lambertian object (SphereOptics) to acquire S_O . S_M was, subsequently, acquired with no filter in the beam path. The computed relative transfer function H_{ab}/H_{abm} is, therefore, a measure of the double-pass transmission of the sample field through each filter, which is equivalent to the single-pass transmission of the laser intensity, as measured independently with a spectrometer (OceanOptics USB2000). The TFT used was an SFFT with a rectangular window, and spatial averaging was performed over 2 mm in x and 400 μm in z . The results of (17) are compared against an uncorrected calculation in which the subtraction of the TFT terms on the right side of the numerator and denominator is omitted.

As expected, the shot noise correction results in a more accurate estimation of the transmission spectra of the optical filter, in comparison to simple normalization. This is particularly evident at the edges of the incident light spectrum, where the noise term becomes more dominant.

We should note that other corrections might be warranted. Unbalanced dispersion between reference and sample arms (such as that arising from light penetrating deep into a dispersive object) causes a sharp depth-varying wavelength dependence over scattering structures [34], which is observed if fine axial resolution is required. Chromatic aberrations arise from the imaging lens [27], which add a focus position dependence to H_{ss} . Also, we find that in line-camera-based detection, the modulation transfer function (MTF) may not be constant across the entire spectrum (due to misalignment of the camera axis), which applies an additional transfer function $H_c(\omega, z)$ onto the time-frequency signal. These latter effects (chromatic focusing and MTF) can be corrected by careful control of the S_M and S_O measurements.

III. SOCT FOR TISSUE ANALYSIS

In OCT, everything known about the object arises from measurement of the reflected (backscattered) light. Physically, backscattering arises from spatial inhomogeneities in the refractive index, such as that which occurs at the locations of boundaries or particles. In tissue, most optical backscattering occurs from subcellular organelles and intracellular structures including the nuclei, mitochondria, cell membranes, fibrous components of the cytoskeleton, and extracellular matrices. In some types of cells, the dominant backscatterers are of a size scale similar to the wavelength of light (Mie scattering regime), in which case their backscattering spectral amplitudes $|H_b(\omega)|$ are highly modulated. The first measurements of tissue backscattering spectra were employed using light-scattering spectroscopy (LSS) [35], where a carefully designed light delivery and probe system can distinguish the singly backscattered light from the multiply scattered diffuse background. By fitting the acquired spectrum with the Mie theory predictions, the size and density of scatterers in the tissue can be analyzed. These measurements have been shown to correlate with premalignant (dysplastic) changes in epithelial cells [3].

Interferometric detection of backscattering spectra (using OCT or low-coherence interferometry (LCI)) allows depth resolution and greater depth penetration than the surface layers accessible with LSS [36]. However, in the typical OCT geometry, only directly backscattered photons within the numerical aperture (NA) of the imaging lens are collected, whereas, in LSS, additional information may be obtained by angular scanning [37]. Angular LCI is the interferometric analog of angular LSS [38], and has proven increasingly useful for detecting nuclear enlargement of epithelial cells, which is a hallmark of cancer development [4]. Having said that, OCT in the backscattering geometry has the potential to image these morphological hallmarks of disease in 3-D, which will be the focus of this discussion.

One of the main challenges in OCT analysis of spectroscopic backscattering is speckle [29]. The measured sample electric field is a coherent superposition of fields scattered from particles within the beam coherence volume [39]. For low NAs and/or the use of spatially incoherent beams, such as in some LSS setups, the spectroscopic response is averaged over a large number of scatterers. In OCT, however, moderate focusing is employed, which results in a small number of scatterers contributing to the response. On the other hand, optical coherence microscopy (OCM) employs high NA optics and tightly focused beams, which, while they can resolve individual scatterers, complicate the analysis of the backscattering response because of the large angular extent of the beam delivery and collection [39].

The speckle noise in standard SOCT can be partially overcome by sufficient incoherent averaging; this has been investigated for structural OCT imaging by diversity methods, such as phase modulation or angular compounding. In the demonstration reported here, this effect is achieved by spatial averaging (incoherently summing the spectral amplitudes).

To demonstrate the feasibility of SOCT-based scatterer sizing, two tissue phantoms were prepared with polystyrene microspheres of diameter 3 and 6 μm (Bangs Laboratories,

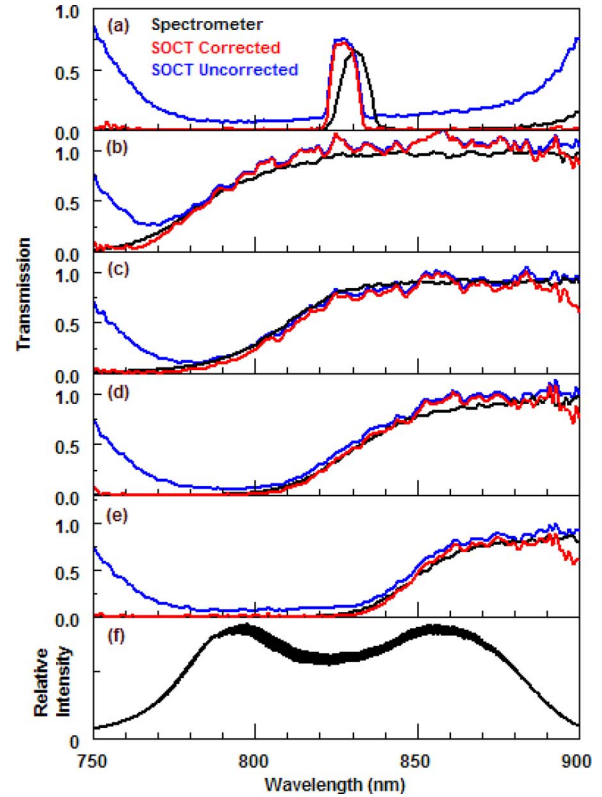


Fig. 2. Comparison between transmission spectra of optical filters measured with a spectrometer and SOCT, using a method which subtracts the lowest order shot noise contribution (corrected) and a simple normalization method (uncorrected). (a) 830-nm 10-nm bandpass filter. (b) 780-nm low-pass filter. (c) 800-nm low-pass filter. (d) 825-nm low-pass filter. (e) 840-nm low-pass filter. (f) Reference beam spectrum $S_R(\omega)$. The bandpass interference filter was tilted for SOCT to avoid strong backreflection, which blue-shifted its frequency response.

Fishers, IN) each with volume densities of 2%. The phantom matrix consisted of 5% gelatin (which quenched the Brownian motion of the microspheres) and 20% glycerol in water. The ratio of the refractive index between microspheres and matrix was 1.19. Moderate focusing was employed (beam waist radius $w_0 \approx 12\lambda$) and the average number of particles per imaging volume was approximately 6.4 and 0.8 for the 3- and 6- μm microspheres, respectively. (Here, we define the imaging volume by the transverse beam extent and the axial extent of the STFT window, which was chosen to be 23 μm .) The time-domain OCT imaging system consisted of the same hardware as the spectral-domain experiment, described earlier for Fig. 2, except that a moving delay arm was used, and the output of the interferometer was dual-balanced with the original laser beam at a photodetector (New Focus 2007, San Jose, CA). For SOCT analysis, an STFT was used with a window length corresponding to 30 μm in air.

The results of SOCT imaging of the microspheres are shown in Fig. 3. A qualitative agreement is obtained between the recovered spectra $|H_b(\omega)|$ and predictions based on the vector Mie theory (accounting for the focusing of the imaging lens). Importantly, the apparent modulation frequency (or pitch) of the spectra is well-matched with theory. This pitch is directly proportional to the scatterer size (as seen by the higher pitch

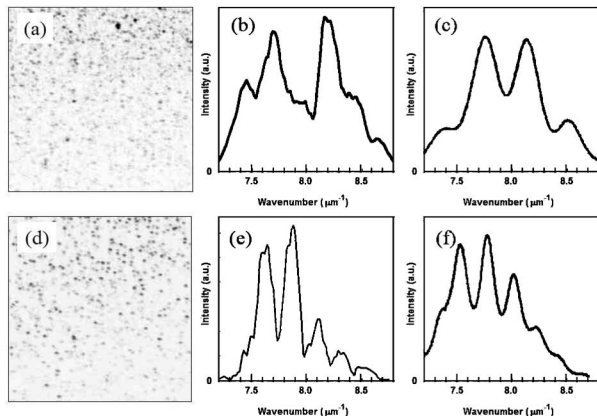


Fig. 3. SOCT analysis of 3 μm (top row) and 6 μm (bottom row) polystyrene microspheres suspended in a gelatin phantom. (a) and (d) are OCT images. (b) and (e) are corresponding SOCT spectra averaged around the beam focus. (c) and (f) are predicted spectra based on vector Mie theory.

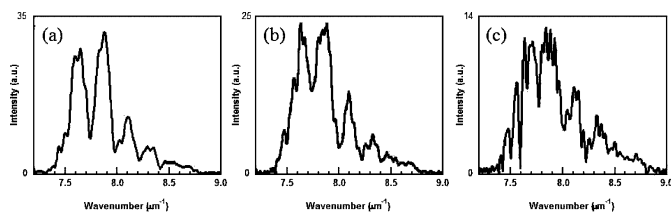


Fig. 4. SOCT spectra of a 6- μm polystyrene sphere in a background of multiple 0.3- μm spheres. (a) Beam centered on a 6- μm sphere. (b) Beam offset from center by w_0 . (c) Beam offset from center by $2w_0$.

evident for the 6- μm microspheres in comparison to the 3- μm ones). Therefore, one way to predict the scatterer size is by taking the magnitude of the Fourier transform of $|H_b(\omega)|$ and measuring the pitch.

In a prototypical biological sample, one might expect to encounter one large scatterer (cell nucleus) surrounded by several small scatterers (mitochondria or other organelles) within the imaging volume. To approximate this effect, we prepared another gelatin phantom with 6- and 0.3- μm polystyrene spheres embedded in the same sample, each with volume densities of 1%. A 3-D imaging volume was acquired with a step size of 1 μm along both transverse axes. The center of a single 6- μm scatterer was located by the maximum scattering point.

In Fig. 4, we can observe the relative contributions of the 6- μm scatterer (large amplitude modulations) and the multiple 0.3- μm scatterers (which are essentially Rayleigh scatterers and only add a noisy offset to the spectrum.) As the beam is scanned transversely off the center of the single large scatterer, the relative contribution of the multitudinous small scatterers increases, as previously predicted [39].

In contrast to the spectral amplitude, the spectral phase can also be used for scatterer sizing. In particular, the RGD may be computed from the phase using (5). RGD is a useful metric as it is highly spectrally modulated for the Mie scatterers, with a pitch that is sensitive to scatterer size. In [40], good agreement is achieved between theoretical and measured RGD spectra for microspheres using OCT. Combining amplitude- and phase-based

measurements may potentially provide even greater sensitivity to particle sizing.

So far, in this section, we have only analyzed the SOCT spectra qualitatively. To present a functional image, it is necessary to first compute the metric (in this case, scatterer size) by some method, and then map this metric to a pixel intensity and color to render a meaningful display. For computing the metric, we earlier mentioned computing $|F(|H_b(\omega)|)|$ and finding the peak pitch value, which is directly proportional to the sphere diameter. However, this method, in practice, may be difficult to implement, as the peak is often not easily distinguished from the low-frequency components (especially, if only a few modulations are present across the light bandwidth). A more robust method is to compute the autocorrelation of the spectrum and measure its correlation width (central lobe). As described in [34], the autocorrelation method is insensitive to Doppler shifts (such as moving delay arm irregularities in time-domain OCT) as well as dispersion, which causes a depth-dependent frequency chirp. In addition to scatterer size, the autocorrelation width is affected by the statistics of the particle distribution within the imaging volume. Larger numbers of scatterers translate into a lower autocorrelation width.

Other techniques for mapping SOCT data into a meaningful SOCT image should be noted. The first was computation of the spectral centroid [13], which is particularly useful for the identification of dyes that preferentially absorb on one side of the light spectrum [41]. This metric is usually assigned to hue in a hue-saturation-value (HSV, where value is also known as luminance) colormap because it is evocative of the spectral shifting. Subsequently, saturation is assigned to the overall backscattering intensity, and, in some cases, luminance as well [34]. The HSV colorspace is also helpful for visualizing the other metrics, such as autocorrelation, as we will demonstrate in Fig. 5. Another method related to centroid mapping is metameric imaging, where the spectrum is divided into three channels and the intensity in each channel is assigned to red, green, and blue [42]. Interestingly, the metameric technique mimics the physical way in which the human eye detects color.

We wished to determine the merits of these techniques for the discrimination of cell types *in vitro*. OCT is particularly useful for imaging and tracking cells in tissue cultures composed of 3-D cell scaffolds [43], because it affords greater depth penetration than microscopy. Although it is possible to label cells with imaging agents for OCT contrast [44], it would be less invasive to directly detect the cell type without modification, purely based on its morphology, which gives rise to a specific scattering spectrum. Our first tests were conducted on two 3-D cell scaffolds (Matrigel, BD Biosciences), which contained either fibroblasts (murine, 3T3 Swiss albino) or macrophages (murine, J774 A.1). Fibroblasts are morphologically elongated in both overall cell shape and nucleus. In contrast, macrophages are generally more isotropic in nature (with pseudopods that extend in random directions). Based on previous works in LCI [45], we expect that nuclear morphology will play a significant role in the SOCT response.

As shown in Fig. 5, the morphological differences between fibroblasts and macrophages appear to correspond to

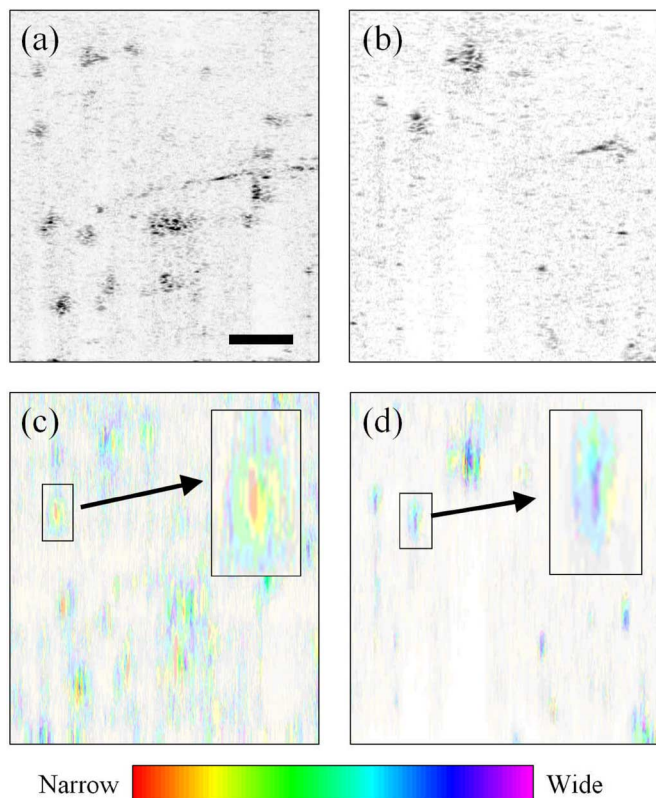


Fig. 5. OCT images (top row) and corresponding SOCT images (bottom row) of cells in a 3-D scaffold. The SOCT images use an HSV colormap where hue is mapped to the 80% autocorrelation width of the local spectrum (scale shown) and saturation is mapped to the OCT intensity. (a) and (c) are macrophages. (b) and (d) are fibroblasts. Boxed insets are $3\times$ magnification. Scalebar $50\ \mu\text{m}$.

qualitative differences between the SOCT images. While many of the macrophages are indicated by a reddish center indicative of a smaller autocorrelation width, the fibroblasts appear to have larger autocorrelation widths, on average. In comparison, there is no observable contrast between cells in the structural OCT image. However, further study is necessary to determine the statistical significance of these observations.

Earlier, we mentioned a drawback of high-NA imaging in terms of complicating the backscattering response. However, OCM has an important advantage. The high-NA lens effectively applies a confocal window to the object response, which is independent of the coherence gate. The consequence of this is that the time-frequency tradeoff, which regulates the coherence gate, is not affected by a shorter confocal window, and, thus, the full spectral resolution may be maintained while only efficiently collecting light from scatterers within a small Δz [42]. One caveat to this, however, is that the ability to interferometrically reject multiply scattered light is determined by the length of the coherence gate, even when using a shorter confocal window. Nevertheless, the spectroscopic OCM technique has shown the ability to localize cell nuclei [42]. We also note that high-NA spectroscopic scattering imaging has previously been investigated with noninterferometric LSS-type systems [46], [47]. These techniques may be useful for functionally monitoring subcellular organelles beyond the usual capabilities of light microscopy.

So far, in this section, our discussion has focused on measurements of spectroscopic scattering for tissue analysis. Likewise, tissue absorption by endogenous chromophores reveals other functional information. One such application is measuring the oxygen saturation (SO_2) of hemoglobin in blood based on its SO_2 -dependent absorption spectrum [48], [49]. Although other photonic methods for pulse oximetry are currently employed, SOCT has the potential to assess SO_2 over a small imaging volume (such as a single blood vessel).

IV. SOCT IMAGING OF CONTRAST AGENTS

While endogenous imaging contrast is preferred over the invasive introduction of exogenous contrast agents, there are only a limited number of endogenous chromophores active in the NIR region. Thus, we turn our attention to chemical agents and small particles that are likely to have low toxicity in tissues, to minimize their complications for *in vivo* use. While the ultimate goal is to specifically image endogenous molecules (such as cell surface receptors indicative of disease), at this relatively early stage, most investigations have focused on the design of agents and imaging techniques just to obtain sensitivity to the agents. Overcoming the tissue backscattering and attenuation background in OCT is a momentous task, especially if little *a priori* information is known. It, thus, remains to be shown that these agents can be surface-modified to provide imaging specificity to the target. However, we direct the reader to the wealth of research in other molecular contrast imaging modalities [5], which demonstrate much progress toward this goal.

One of the most obvious platforms for spectroscopic contrast is the use of NIR-active dyes. As shown in [41], a dye with peak wavelength on the blue side of the light source spectrum was used to provide SOCT contrast. As light passes through the dye, the shorter wavelengths are absorbed and the detected spectrum shifts toward longer wavelengths. By computing the centroid shift of the total SOCT response, the relative concentration of dye within a botanical stem (celery stalk) was imaged, as shown in Fig. 6. Another method for imaging dyes has been demonstrated based on spectral triangulation, in which three successive images are obtained at different laser central wavelengths [50]. Although this process is somewhat cumbersome, it was capable of tracking a dye (indocyanine green) within a living specimen. We note that indocyanine green is a promising SOCT agent as it has received FDA approval for certain applications. As mentioned in Section II, it is possible to use the entire imaging spectrum to estimate the dye concentration in a least-squares sense [28]. This least-squares method has been validated in turbid multilayer phantoms. Beyond molecular contrast imaging, another important application of absorption contrast imaging is to monitor the diffusion of photosensitizers used in photodynamic therapy (PDT) [32].

Plasmon-resonant nanoparticles comprise another major class of contrast agents for OCT. In particular, anisotropic or layered gold particles exhibit strong resonances in the NIR, and gold is also a good material due to its potential biocompatibility. Generally, larger particles ($>100\ \text{nm}$) exhibit resonant

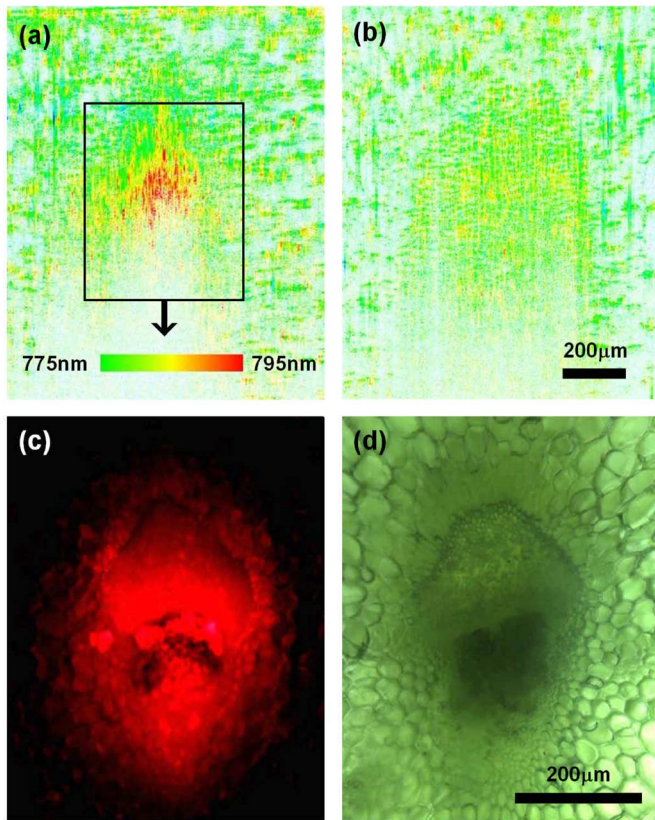


Fig. 6. NIR dye contrast in a celery stalk using SOCT and fluorescence microscopy, reprinted from [41]. (a) and (b) are SOCT images of the celery with and without dye, respectively. Scalebars as shown. (c) Fluorescence microscopy corresponding to the boxed region of (a) showing dye localization in the central vascular bundle, size scale same as (d). (d) Light microscopy corresponding to (a) showing the vascular bundle and surrounding collenchyma tissue.

scattering effects, whereas Rayleigh particles (< 100 nm) are dominated by absorption. The potential for these types of agents for spectroscopic-based contrast, and, in particular, for colorimetric assays, has long been recognized [51]. However, it was only recently that spectroscopic contrast was demonstrated in SOCT [52], using a structured particle known as a nanocage. Nanocages, approximately 35 nm in size and exhibiting an absorption peak of 716 nm, were imaged within an agarose gel phantom (using the standard HSV centroid mapping [13].) Nanoshells are another interesting construct composed of a silica core and a gold shell. They can be designed either for spectroscopic scattering or absorption applications [53], although, to date, they have been primarily used for their overall scattering enhancement in standard OCT [54], [55]. Finally, nanorods are rod-shaped particles that can be batch synthesized with extremely small volumes (~ 6000 nm³) for applications where tissue mobility is important. Nanorods of gold have been demonstrated with standard OCT contrast using a backscattering albedo metric [30]. We will also show their potential as SOCT contrast agents here.

To understand the sensitivity of detection of absorbing contrast agents in a scattering-dominated tissue medium, we performed SOCT imaging on 2% intralipid solutions (as a tissue phantom) with small dosages of plasmon-resonant nanorods

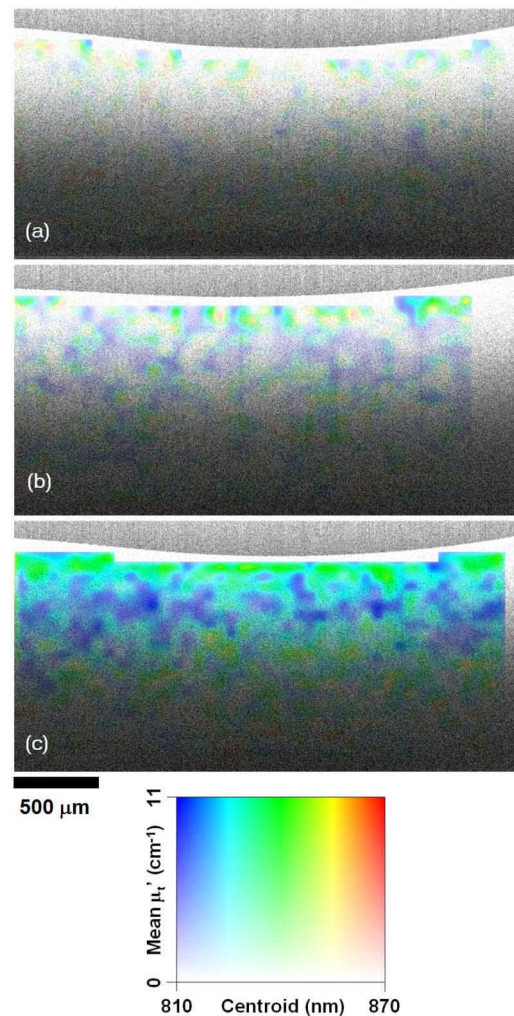


Fig. 7. SOCT images of 2% intralipid (a) without nanorods, (b) with nanorods of 7.2-cm⁻¹ peak attenuation, (c) with nanorods of 18-cm⁻¹ peak attenuation. Hue and saturation mapping are indicated by the scalebox, and luminance is mapped to the structural OCT image.

added. These gold nanorods of ~ 15 nm \times 45-nm dimension were synthesized by previously published methods [56]. The nanorods exhibited an absorption maximum at 755 nm and full-width at half-maximum of 135 nm. Thus, the absorption band of these nanorods extended into the blue side of the laser bandwidth centered at 800 nm (with the same spectrum as in Fig. 2.) The spectral-domain OCT system and processing method described earlier were used in this study. The cumulative attenuation coefficient μ_t from the top surface was estimated using (13), where the response in the immediate vicinity of the surface was removed due to noise. The reference object used to measure S_M in (17) was the 2% intralipid sample without nanorods. However, because of the chromatic focusing aberration, it was necessary to also parameterize the top surface position in the S_M data (because the focus axial position shifts as the top surface shifts). Thus, in the S_O images, where the top surface extends beyond the range characterized by S_M , no spectroscopic data was computed (seen as color-free vertical stripes in Fig. 7).

For the visualization of the SOCT data, shown in Fig. 7, a different HSV mapping was used. In this case, the spectral attenuation coefficient $\mu_t(\omega)$ (not $|H_{ab}|$) was used as the metric. Its centroid wavelength was computed and assigned to hue, and its total integrated amplitude was computed and assigned to saturation, finally assigning luminance to the structural OCT image intensity. Also, the hue-saturation channels were spatially filtered to reduce speckle noise.

As shown in Fig. 7, as the concentration of nanorods is increased, attenuation is added at the blue wavelengths, which accordingly shifts the centroid of the measured spectral attenuation coefficient $\mu_t(\omega)$. However, for z too close to the intralipid surface, there is insufficient cumulative absorption for this effect to be observed. As the maximum penetration depth of the light is reached, the estimate of μ_t also becomes noisy. Overall, we find that the concentration of nanorods required to observe an effect at the intermediate depths (Fig. 7b) is of the order of 100 ppm by weight, which is comparable to the sensitivity achieved using alternate techniques [30]. Future improvements in the size and shape distribution of the nanorods could theoretically provide an absorption peak with around four times the extinction values measured in this study. As noted in [30], this concentration may be sufficient for detecting cell surface receptors targeted with nanorods.

V. CONCLUSION

In summary, this paper reviews the major signal processing algorithms and biomedical applications that advance spectroscopic OCT. As with most engineering applications, there are many design tradeoffs (both in hardware and software) that should be considered with regard to the scientific question that the SOCT instrumentation and techniques will be used to answer. There is no one SOCT system that works for all imaging scenarios. The major choices to be considered are the imaging lens NA, light source bandwidth, time-frequency transformation, computation of the appropriate metric(s), incoherent signal averaging, and multichannel image display.

Fortunately, many of these choices have already been made for a variety of specific applications. Spectroscopic scattering measurements are increasingly used for scatterer sizing, providing contrast to morphological differences in biological cells. Molecular contrast imaging using spectroscopic contrast agents is an area poised for advance. Clearly, there is a seemingly infinite variety of scientific inquiries that can be addressed with molecular or functional imaging using SOCT techniques.

ACKNOWLEDGMENT

The authors would like to thank Prof. A. Wei and M. N. Hansen from the Department of Chemistry at Purdue University for production of the plasmon-resonant gold nanorods, and Dr. D. L. Marks, Dr. T. S. Ralston, E. J. Chaney, and J. L. Chin from the Beckman Institute for Advanced Science and Technology at the University of Illinois at Urbana-Champaign, for their technical input and laboratory assistance.

REFERENCES

- [1] Y. Mendelson, "Pulse oximetry: Theory and applications for noninvasive monitoring," *Clin. Chem.*, vol. 38, no. 9, pp. 1601–1607, 1992.
- [2] A. S. Haka, Z. Volynskaya, J. A. Gardecki, J. Nazemi, J. Lyons, D. Hicks, M. Fitzmaurice, R. R. Dasari, J. P. Crowe, and M. S. Feld, "In vivo margin assessment during partial mastectomy breast surgery using Raman spectroscopy," *Cancer Res.*, vol. 66, no. 6, pp. 3317–3322, 2006.
- [3] V. Backman, M. B. Wallace, L. T. Perelman, J. T. Arendt, R. Gurjar, M. G. Muller, Q. Zhang, G. Zonios, E. Kline, T. McGillican, S. Shapshay, T. Valdez, K. Badizadegan, J. M. Crawford, M. Fitzmaurice, S. Kabani, H. S. Levin, M. Seiler, R. R. Dasari, I. Itzkan, J. Van Dam, and M. S. Feld, "Detection of preinvasive cancer cells," *Nature*, vol. 406, no. 6791, pp. 35–36, 2000.
- [4] A. Wax, J. W. Pyhtila, R. N. Graf, R. Nines, C. W. Boone, R. R. Dasari, M. S. Feld, V. E. Steele, and G. D. Stoner, "Prospective grading of neoplastic change in rat esophagus epithelium using angle-resolved low-coherence interferometry," *J. Biomed. Opt.*, vol. 10, no. 5, p. 051604, 2005.
- [5] T. F. Massoud and S. S. Gambhir, "Molecular imaging in living subjects: Seeing fundamental biological processes in a new light," *Genes Dev.*, vol. 17, pp. 545–580, 2003.
- [6] M. D. Duncan, J. Reintjes, and T. J. Manuccia, "Scanning coherent anti-Stokes Raman microscope," *Opt. Lett.*, vol. 7, no. 8, pp. 350–352, 1982.
- [7] D. L. Marks and S. A. Boppart, "Nonlinear interferometric vibrational imaging," *Phys. Rev. Lett.*, vol. 92, no. 12, p. 123905, 2004.
- [8] E. O. Potma, C. L. Evans, and X. S. Xie, "Heterodyne coherent anti-Stokes Raman scattering (CARS) imaging," *Opt. Lett.*, vol. 31, no. 2, pp. 241–243, 2006.
- [9] J. S. Bredfeldt, C. Vinegoni, D. L. Marks, and S. A. Boppart, "Molecularly sensitive optical coherence tomography," *Opt. Lett.*, vol. 30, no. 5, pp. 495–497, 2005.
- [10] F. Legare, C. L. Evans, F. Ganikhanov, and X. S. Xie, "Toward CARS endoscopy," *Opt. Express*, vol. 14, no. 10, pp. 4427–4432, 2006.
- [11] D. Huang, E. A. Swanson, C. P. Lin, J. S. Schuman, W. G. Stinson, W. Chang, M. R. Hee, T. Flotte, K. Gregory, C. A. Puliafito, and J. G. Fujimoto, "Optical coherence tomography," *Science*, vol. 254, no. 5035, pp. 1178–1181, 1991.
- [12] M. D. Kulkarni and J. A. Izatt, "Spectroscopic optical coherence tomography," in *Conf. Lasers Electro-Opt., OSA Tech. Dig. Ser.*, 1996, pp. 59–60.
- [13] U. Morgner, W. Drexler, F. C. Kartner, X. D. Li, C. Pitris, E. P. Ippen, and J. G. Fujimoto, "Spectroscopic optical coherence tomography," *Opt. Lett.*, vol. 25, no. 2, pp. 111–113, 2000.
- [14] S. A. Boppart, A. L. Oldenburg, C. Xu, and D. L. Marks, "Optical probes and techniques for molecular contrast enhancement in coherence imaging," *J. Biomed. Opt.*, vol. 10, no. 4, 041208, 2005.
- [15] A. F. Fercher, W. Drexler, C. K. Hitzenberger, and T. Lasser, "Optical coherence tomography—principles and applications," *Rep. Prog. Phys.*, vol. 66, pp. 239–303, 2003.
- [16] R. Loudon, *The Quantum Theory of Light*. New York: Oxford University Press, 1984, pp. 83–84.
- [17] V. Laude, "Noise analysis of the measurement of group delay in Fourier white-light interferometric cross correlation," *J. Opt. Soc. Am. B, Opt. Phys.*, vol. 19, no. 5, pp. 1001–1008, 2002.
- [18] R. Leitgeb, C. K. Hitzenberger, and A. F. Fercher, "Performance of Fourier domain vs. time domain optical coherence tomography," *Opt. Express*, vol. 11, no. 8, pp. 889–894, 2003.
- [19] J. F. de Boer, B. Cense, B. H. Park, M. C. Pierce, G. J. Tearney, and B. E. Bouma, "Improved signal-to-noise ratio in spectral-domain compared with time-domain optical coherence tomography," *Opt. Lett.*, vol. 28, no. 21, pp. 2067–2069, 2003.
- [20] S. R. Chinn, E. A. Swanson, and J. G. Fujimoto, "Optical coherence tomography using a frequency-tunable optical source," *Opt. Lett.*, vol. 22, no. 5, pp. 340–342, 1997.
- [21] N. Tan-no, T. Ichimura, T. Funaba, N. Anndo, and Y. Odagiri, "Optical multimode frequency-domain reflectometer," *Opt. Lett.*, vol. 19, no. 8, pp. 587–589, 1994.
- [22] R. Leitgeb, M. Wojtkowski, A. Kowalczyk, C. K. Hitzenberger, M. Sticker, and A. F. Fercher, "Spectral measurement of absorption by spectroscopic frequency-domain optical coherence tomography," *Opt. Lett.*, vol. 25, no. 11, pp. 820–822, 2000.
- [23] C. Xu, F. Kamalabadi, and S. A. Boppart, "Comparative performance analysis of time-frequency distributions for spectroscopic optical coherence tomography," *Appl. Opt.*, vol. 44, no. 10, pp. 1813–1822, 2005.

- [24] I. Daubechies, "The wavelet transform, time-frequency localization and signal analysis," *IEEE Trans. Inf. Theory*, vol. 36, no. 5, pp. 961–1005, Sep. 1990.
- [25] L. Cohen, "Time-frequency distributions—A review," in *Proc. IEEE*, 2007, vol. 77, no. 7, pp. 941–981, Jul. 1989.
- [26] R. N. Graf and A. Wax, "Temporal coherence and time-frequency distribution in spectroscopic optical coherence tomography," *J. Opt. Soc. Am. A, Opt. Image*, vol. 24, no. 8, pp. 2186–2195, 2007.
- [27] B. Hermann, K. Bizheva, A. Unterhuber, B. Povazay, H. Sattmann, L. Schmetterer, A. F. Fercher, and W. Drexler, "Precision of extracting absorption profiles from weakly scattering media with spectroscopic time-domain optical coherence tomography," *Opt. Express*, vol. 12, no. 8, pp. 1677–1688, 2004.
- [28] C. Xu, D. L. Marks, M. N. Do, and S. A. Boppart, "Separation of absorption and scattering profiles in spectroscopic optical coherence tomography using a least-squares algorithm," *Opt. Express*, vol. 12, no. 2, pp. 4790–4803, 2004.
- [29] J. M. Schmitt, S. H. Xiang, and K. M. Yung, "Speckle in optical coherence tomography," *J. Biomed. Opt.*, vol. 4, no. 1, pp. 95–105, 1999.
- [30] A. L. Oldenburg, M. N. Hansen, D. A. Zweifel, A. Wei, and S. A. Boppart, "Plasmon-resonant gold nanorods as low backscattering albedo contrast agents for optical coherence tomography," *Opt. Express*, vol. 14, no. 15, pp. 6724–6738, 2006.
- [31] D. Levitz, L. Thrane, M. H. Frosz, P. E. Andersen, C. B. Andersen, J. Valanciunaite, J. Swartling, S. Andersson-Engels, and P. R. Hansen, "Determination of optical scattering properties of highly-scattering media in optical coherence tomography images," *Opt. Express*, vol. 12, no. 2, pp. 249–259, 2004.
- [32] T. Støren, A. Royset, L. O. Svaasand, and T. Lindmo, "Functional imaging of dye concentration in tissue phantoms by spectroscopic optical coherence tomography," *J. Biomed. Opt.*, vol. 10, no. 2, 024037, 2005.
- [33] T. S. Ralston, D. L. Marks, P. S. Carney, and S. A. Boppart, "Interferometric synthetic aperture microscopy," *Nat. Phys.*, vol. 3, no. 2, pp. 129–134, 2007.
- [34] D. C. Adler, T. H. Ko, P. R. Herz, and J. G. Fujimoto, "Optical coherence tomography contrast enhancement using spectroscopic analysis with spectral autocorrelation," *Opt. Express*, vol. 12, no. 22, pp. 5487–5501, 2004.
- [35] L. T. Perelman, V. Backman, M. Wallace, G. Zonios, R. Manoharan, A. Nusrat, S. Shields, M. Seiler, C. Lima, T. Hamano, I. Itzkan, J. Van Dam, J. M. Crawford, and M. S. Feld, "Observation of periodic fine structure in reflectance from biological tissue: A new technique for measuring nuclear size distribution," *Phys. Rev. Lett.*, vol. 30, no. 3, pp. 627–630, 1998.
- [36] C. Yang, L. T. Perelman, A. Wax, R. R. Dasari, and M. S. Feld, "Feasibility of field-based light scattering spectroscopy," *J. Biomed. Opt.*, vol. 5, no. 2, pp. 138–143, 2000.
- [37] Y. L. Kim, Y. Liu, R. K. Wali, H. K. Roy, M. J. Goldberg, A. K. Kromin, K. Chen, and V. Backman, "Properties of light scattering for characterization of tissue microarchitecture and its alteration in early precancer," *IEEE J. Sel. Topics Quantum Electron.*, vol. 9, no. 2, pp. 243–256, Mar.–Apr. 2003.
- [38] J. W. Pyhtila, R. N. Graf, and A. Wax, "Determining nuclear morphology using an improved angle-resolved low coherence interferometry system," *Opt. Express*, vol. 11, no. 25, pp. 3473–3484, 2003.
- [39] C. Xu, P. S. Carney, and S. A. Boppart, "Wavelength-dependent scattering in spectroscopic optical coherence tomography," *Opt. Express*, vol. 13, no. 14, pp. 5450–5462, 2005.
- [40] S. D. Dyer, T. Dennis, L. K. Street, S. M. Etzel, T. A. Germer, and A. Diestfey, "Spectroscopic phase-dispersion optical coherence tomography measurements of scattering phantoms," *Opt. Express*, vol. 14, no. 18, pp. 8138–8153, 2006.
- [41] C. Xu, J. Ye, D. L. Marks, and S. A. Boppart, "Near-infrared dyes as contrast-enhancing agents for spectroscopic optical coherence tomography," *Opt. Lett.*, vol. 29, no. 14, pp. 1647–1649, 2004.
- [42] C. Xu, C. Vinegoni, T. S. Ralston, W. Luo, W. Tan, and S. A. Boppart, "Spectroscopic spectral-domain optical coherence microscopy," *Opt. Lett.*, vol. 31, no. 8, pp. 1079–1081, 2006.
- [43] W. Tan, A. L. Oldenburg, J. J. Norman, T. A. Desai, and S. A. Boppart, "Optical coherence tomography of cell dynamics in three-dimensional tissue models," *Opt. Express*, vol. 14, no. 16, pp. 7159–7171, 2006.
- [44] A. L. Oldenburg, J. R. Gunther, and S. A. Boppart, "Imaging magnetically labeled cells with magnetomotive optical coherence tomography," *Opt. Lett.*, vol. 30, no. 7, pp. 747–749, 2005.
- [45] R. N. Graf and A. Wax, "Nuclear morphology measurements using Fourier domain low coherence interferometry," *Opt. Express*, vol. 13, no. 12, pp. 4693–4698, 2005.
- [46] H. Fang, L. Qiu, E. Vitkin, M. M. Zaman, C. Andersson, S. Salahuddin, L. M. Kimerer, P. B. Cipolloni, M. D. Modell, B. S. Turner, S. E. Keates, I. Bigio, I. Itzkan, S. D. Freedman, R. Bansil, E. B. Hanlon, and L. T. Perelman, "Confocal light absorption and scattering spectroscopic microscopy," *Appl. Opt.*, vol. 46, no. 10, pp. 1760–1769, 2007.
- [47] Y. Liu, X. Li, Y. L. Kim, and V. Backman, "Elastic backscattering spectroscopic microscopy," *Opt. Lett.*, vol. 30, no. 18, pp. 2445–2447, 2005.
- [48] D. J. Faber, E. G. Mik, M. C. G. Aalders, and T. G. van Leeuwen, "Light absorption of (oxy-)hemoglobin assessed by spectroscopic optical coherence tomography," *Opt. Lett.*, vol. 28, no. 16, pp. 1436–1438, 2003.
- [49] D. J. Faber, E. G. Mik, M. C. G. Aalders, and T. G. van Leeuwen, "Toward assessment of blood oxygen saturation by spectroscopic optical coherence tomography," *Opt. Lett.*, vol. 30, no. 9, pp. 1015–1017, 2005.
- [50] C. Yang, L. E. L. McGuckin, J. D. Simon, M. A. Choma, B. E. Applegate, and J. A. Izatt, "Spectral triangulation molecular contrast optical coherence tomography with indocyanine green as the contrast agent," *Opt. Lett.*, vol. 29, no. 17, pp. 2016–2018, 2004.
- [51] J. L. West and N. J. Halas, "Engineered nanomaterials for biophotonics applications: Improving sensing, imaging, and therapeutics," *Annu. Rev. Biomed. Eng.*, vol. 5, pp. 285–292, 2003.
- [52] H. Cang, T. Sun, and Z.-Y. Li, "Gold nanocages as contrast agents for spectroscopic optical coherence tomography," *Opt. Lett.*, vol. 30, no. 22, pp. 3048–3050, 2005.
- [53] A. M. Gobin, M. H. Lee, N. J. Halas, W. D. James, R. A. Drezek, and J. L. West, "Near-infrared resonant nanoshells for combined optical imaging and photothermal cancer therapy," *Nano Lett.*, vol. 7, no. 7, pp. 1929–1934, 2007.
- [54] A. W. H. Lin, N. A. Lewinski, J. L. West, N. J. Halas, and R. A. Drezek, "Optically tunable nanoparticle contrast agents for early cancer detection: Model-based analysis of gold nanoshells," *J. Biomed. Opt.*, vol. 10, no. 6, 064035, 2005.
- [55] A. Agarwal, S. Huang, A. W. H. Lin, M.-H. Lee, J. K. Barton, R. A. Drezek, and T. J. Pfefer, "Quantitative evaluation of optical coherence tomography signal enhancement with gold nanoshells," *J. Biomed. Opt.*, vol. 11, no. 4, 041121, 2006.
- [56] D. A. Zweifel and A. Wei, "Sulfide-arrested growth of gold nanorods," *Chem. Mater.*, vol. 17, pp. 4256–4261, 2005.



Amy L. Oldenburg was born in the suburbs of Chicago, IL, in 1974. She received a diploma from the Illinois Mathematics and Science Academy, Aurora, in 1991, the B.S. (Hons.) degree in applied physics from the California Institute of Technology, Pasadena, in 1995, and the M. S. and Ph.D. degrees in physics from the University of Illinois at Urbana-Champaign, Urbana, in 1997 and 2001, respectively.

As a Graduate Research Assistant, she was engaged in research on atomic and diatomic alkali vapor dynamics using femtosecond laser pulses to generate electronic wavepackets. In 2001, she held a Postdoctoral position with the Biophotonics Imaging Laboratory, Beckman Institute for Advanced Science and Technology, University of Illinois at Urbana-Champaign, where she is currently a Senior Research Scientist. Her current research interests include developing novel molecular contrast imaging techniques and associated nanoparticles for use with optical coherence tomography.



Chenyang Xu (S'94–A'99–M'01) was born in China in 1976. He received the B. S. degree in biology from Tsinghua University, Beijing, China, in 1996, and the M.S. degree in biology, another M.S. degree in electrical engineering, and the Ph.D. degree in electrical engineering from the University of Illinois at Urbana-Champaign, Urbana, in 2000, 2001, and 2005, respectively.

In 2005, he joined Lightlab Imaging, Inc., Westford, MA, as a Senior Research Engineer. His current research interests include the development of

optical technology for cardiology diagnosis.



Stephen A. Boppart (S'90–M'90–SM'06) was born in Harvard, IL, in 1968. He received the B.S. degree in electrical and bioengineering and the M.S. degree in electrical engineering in 1990 and 1991, respectively, both from the University of Illinois at Urbana-Champaign, Urbana, the Ph.D. degree in electrical and medical engineering from the Massachusetts Institute of Technology, Cambridge, in 1998, and the M.D. degree from Harvard Medical School, Boston, MA, in 2000. He completed the residency training in internal medicine from the University of Illinois at Urbana-Champaign, in 2005.

Prior to beginning his doctoral work, he was a Research Scientist at the Air Force Laser Laboratory, Brooks Air Force Base, San Antonio, TX, where he was engaged in research on developing national (ANSI) and Air Force laser safety standards. Following his doctoral studies, he returned to the University of Illinois at Urbana-Champaign in 2000, where he is currently an Associate Professor of Electrical and Computer Engineering, Bioengineering, and Inter-

nal Medicine, and Head of the Biophotonics Imaging Laboratory, Beckman Institute for Advanced Science and Technology. He also holds a joint position as Founding Director of the Mills Breast Cancer Institute, Carle Foundation Hospital, Urbana. He is the author or coauthor of more than 130 invited and contributed publications and over 300 invited and contributed presentations. He is the holder of over 15 patents filed or pending. His current research interests include the development of novel optical imaging technologies for biological and medical applications, with particular emphasis on translating these to clinical applications in cancer detection and diagnosis.

Dr. Boppart is a member of the Optical Society of America, SPIE, the Society of Photographic Instrumentation Engineers, the Society for Molecular Imaging, the Academy of Molecular Imaging, the American Association for the Advancement of Science, the American Association for Cancer Research, and the American Medical Association. In 2002, he was named one of the Top 100 Innovators in the World by the Technology Review Magazine for his research in medical technology, and, in 2005, he received the IEEE EMBS Early Career Achievement Award.